Omnidirectional enhancement of photocatalytic hydrogen evolution over hierarchical "cauline leaf" nanoarchitectures

Longlu Wang [a,1], Xidong Duan [a,1], Gongming Wang [b], Chengbin Liu [a,*], Shenglian Luo [a,*], Shuqu Zhang [a], Yunxiong Zeng [a], Yuzi Xu [a], Yutang Liu [c], Xiangfeng Duan [b,*]

[a] State Key Laboratory of Chemo/Biosensing and Chemometrics, Hunan University, Changsha 410082, PR China
[b] Department of Chemistry and Biochemistry, University of California, Los Angeles, CA 90095, USA
[c] College of Environmental Science and Engineering, Hunan University, Changsha 410082, PR China

ABSTRACT

The scrupulous design and integration of multiple active materials into hierarchical nanoarchitectures is essential for the creation of photocatalytic hydrogen evolution reaction (HER) system that can mimic natural photosynthesis. Here we report the design and preparation of a "cauline leaf"-like structure for highly efficient HER, by decorating TiO$_2$ nanofibers with vertical arrays of atomically-thin MoS$_2$ nanosheets and CdS nanocrystals. The unique integrated "cauline leaf" design can promote light trapping and absorption for highly efficient light harvesting and photocarrier generation, and offer unblocked electron transport pathway for rapid charge separation/transport to suppress charge recombination, as well as high surface area and high density of active sites for highly efficient utilization of photo-generated carriers for productive HER. Structural characterizations by transmission electron microscopy show well-integrated nanoarchitectures. Significantly, photocatalytic studies demonstrate rapid HER rates as high as 12.3 or 6.2 mmol h^{-1} g^{-1} under simulated solar light or visible light irradiation, with apparent quantum efficiencies of 70.5% at 365 nm or 57.6% at 420 nm, and excellent long term stability, representing one of the best reported MoS$_2$ hybrid HER photocatalysts. The study could open new opportunities for the rational design of nanoscale architectures for HER or other application.

© 2016 Elsevier B.V. All rights reserved.

1. Introduction

Hydrogen energy is a promising alternative form of clean energy in the future. Loading of noble metal co-catalysts on semiconductors is an attractive way for photocatalytical production of molecular hydrogen, but are severely limited by their scarcity and cost for practical applications [1–3]. Tremendous efforts in recent years have proved that molybdenum disulfide (MoS$_2$) is a potential substitute for platinum [4–6]. The edge sites of MoS$_2$ nanosheets have been revealed to be the active sites for the hydrogen evolution reaction (HER) [7–9]. Generally, the main challenge in heterogeneous photocatalysis toward HER is to minimize the non-productive recombination and efficiently extract the photogenerated charges for productive hydrogen generation. To this end, a close integration of the semiconductor light har-

vesting antenna and hydrogen evolution cocatalysts is essential for ensuring efficient photocharge generation, separation, transport and utilization [10–13]. In particular, when MoS$_2$ nanosheets are used as the cocatalyst, not only the highly intimate interfacial contact between MoS$_2$ and semiconductor is required for the fast separation and transfer of photogenerated charges, but also the catalytically active edge sites of MoS$_2$ nanosheets in hybrid photocatalysts should be fully exposed for efficient HER [14–16]. Frustratingly, unshackled two dimensional transition-metal dichalcogenide nanosheet-based hybrids in solution tend to aggregate, greatly obstructing the exposure of edge active sites [17,18]. The scrupulous design and hybridization of MoS$_2$-based architectures are crucial to HER.

Although considerable efforts have been placed in preparing MoS$_2$ nanosheet-based hybrid photocatalysts [19–22], these pioneering studies are mostly focusing on the simple hybridization of MoS$_2$ nanosheets, without sufficient control of the nanoscale architectures for opitmized performance [14]. On the other hand, it is expected that the HER performance of the catalysts is strongly dependent on their composition, crystal phase and structure, as well as the spatial organization/assembly of components. It is

therefore highly desirable to prepare well-defined MoS_2 hybrid catalysts in a highly controllable fashion [14,23,24].

Here we report the rational design and synthesis of a "cauline leaf"-like structure for highly efficient HER, by decorating 1D TiO_2 nanofibers with a vertical array of atomically-thin 2D MoS_2 nanosheets and 0D CdS nanocrystals (TiO_2@MoS_2@CdS) (Scheme 1). 1D TiO_2 nanofibers have been saved as an ideal scaffold to composite with other homogeneous or heterogeneous MoS_2 nanosheets in order to ensure high surface area, reinforce light scattering and trapping, and suppress unexpected back reaction (charge recombination). 0D CdS nanocrystals anchored on the 2D MoS_2 nanosheets serve as the photocenter for efficiently harvesting solar light to generate charge carriers. The 0D/1D/2D hierarchical nanoarchitectures fully integrate the merits and mitigate the drawbacks of the single units. Such a hierachical "cauline leaf" architecture maximizes omnidirectional enhancement in photocatalytic hydrogen evolution. These results show the importance of morphology control in the preparation of base MoS_2 as cocatalyst for highly efficient photocatalytic hydrogen evolution.

2. Experimental

2.1. Materials

Poly(vinylpyrrolidone) (PVP, Mw = 1,300,000) was purchased from Alfa Aesar. All other reagents and materials were obtained commercially from the Beijing Chemical Reagent (Beijing, China) and used as received without further purification.

2.2. Synthesis of porous electrospun TiO_2 nanofibers

Typically, 0.45 g of PVP was dissolved in 3 mL ethanol with vigorous stirring for 1 h. 1.5 g of titanium tetraiso-propoxide ($Ti(O_iPr)_4$) was dissolved in a mixture of 3 mL ethanol and 3 mL acetic acid by stirring for 1 h to obtain a homogeneous precursor solution, and then the above PVP solution was added to the homogeneous precursor solution, followed by vigorous stirring for 3 h. The mixed solution was put into a syringe for electrospinning. An electrical potential of 10 kV was applied at an electrode distance of 15 cm. The mixed solution was ejected at a rate of 0.5 mL h^{-1}, resulting in electrospun nanofibers. The as-collected nanofibers were calcined at 450 °C for 2 h in air atmosphere to remove PVP with the formation of TiO_2 crystals. PVP acted as here both linkers between the inorganic precursors to facilitate electrospinning and porogenic agents to obtain porous TiO_2 nanofibres after the PVP removal by a calcination process.

2.3. Preparation of TiO_2@MoS_2 heterostructures

The formation process of TiO_2@MoS_2 heterostructures was described below: typically, 45 mg sodium molybdate ($Na_2MoO_4 \cdot 2H_2O$) and 90 mg thioacetamide (C_2H_5NS) were dissolved in 20 mL deionized water to form a transparent solution. Then 20 mg calcined TiO_2 nanofibers were added into the above solution and stirred to get a suspension. The suspension was transferred to a Teflon-lined stainless steel autoclave and then heated in an electric oven at 220 °C for 24 h. The solid product was dried at 80 °C for 12 h to obtain TiO_2@MoS_2 heterostructures (containing 60 wt% of MoS_2). The content of MoS_2 in TiO_2@MoS_2 could be tuned by adjusting the amount of $Na_2MoO_4 \cdot 2H_2O$ and C_2H_5NS precursors, and only the optimized TiO_2@MoS_2 sample containing 60 wt% of MoS_2 was used for analysis in detail unless otherwise stated. For comparison, pure MoS_2 nanosheets were prepared under the same conditions without TiO_2 nanofibers.

2.4. Synthesis of TiO_2@MoS_2@CdS heterostructures

In a typical synthesis process of TiO_2@MoS_2@CdS, 50 mg TiO_2@MoS_2 was dispersed in 50 mL aqueous solution containing 138.38 mg Cd(AC)$_2 \cdot 2H_2O$ by sonication for 8 h. Then 0.05 M $Na_2S \cdot 9H_2O$ was added at the rate of 0.05 mL/min and continuously stirred for 24 h. Finally, the products were washed with distilled water and dried in air at 60 °C. The content of CdS in TiO_2@MoS_2@CdS was tuned by the amount of raw materials. For comparison, pure CdS nanoparticles were prepared by adding sodium sulfide (10 mL, 0.1 mm) to cadmium acetate (10 mL, 0.1 mm) with stirring; the precipitate formed was centrifuged and dried at 60 °C. For comparison, TiO_2@CdS was prepared under the same conditions without MoS_2 nanosheets.

2.5. Characterization

The morphologies and microstructures of the samples were characterized using an S-4800 field emission scanning electron microscope (FESEM, Hitachi, Japan) and a transmission electron microscope (TEM, JEOL JEM-2100F). The EDS mapping images were captured on a Tecnai G2 F20 S-TWIN atomic resolution analytical microscope. The crystal phases of the samples were collected on an X-ray diffractometer with Cu-Kα radiation (XRD, M21X, MAC Science Ltd., Japan). The binding energies of S, Mo, and O of the heterostructures were determined by X-ray photoelectron spectroscopy (XPS, K-Alpha 1063, Thermo Fisher Scientific, England) using an Al-Kα X-ray source. The UV–vis diffuse reflectance spectra (DRS) were performed on a UV–vis spectrophotometer (Cary 300, USA) with an integrating sphere. The photoluminescenece (PL) spectra for solid samples were investigated through F-7000. The time-resolved transient photoluminescence (TRPL) spectrum was performed using Hamamatsu universal streak camera C10910. The BET specific surface areas were measured on Belsorp-Mini II analyser (Japan).

2.6. Photoelectrochemical measurements

The photoelectrochemical responses of the samples were carried out with a CHI 660C electrochemical analyzer (CHI Inc., USA) in a three-electrode configuration. FTO electrodes deposited with the samples as a photoanode, a platinum wire as the counter electrode, and a saturated calomel electrode (SCE) as the reference electrode. All the samples were analyzed under room temperature without bias potential. 0.35 M/0.25 M Na_2S–Na_2SO_3 aqueous solution was used as the electrolyte. For the fabrication of the photoanode, 0.25 g of the sample was grinded with 0.06 g polyethylene glycol (PEG, molecular weight: 20000) and 0.5 ml ethanol to make a slurry. Then, the slurry was coated onto a 1 cm × 4 cm F-doped SnO_2-coated glass (FTO glass) electrode by the doctor blade technique, and then allowed to dry in air. A 300 W xenon arc lamp with lighting wavelength range of 320–780 nm (Perfectlight, PLS-SXE 300C, Beijing, China) was used as light source. The light intensity parameters are provided by Beijing Perfectlight Technology Co., Ltd. (see Fig. S1 in Supporting information). The incident light intensity was 160 mW cm^{-2} measured by a radiometer (FZ-A, Photoelectric Instrument Factory of Beijing Normal University, China).

2.7. Photocatalytic hydrogen production tests

The photocatalytic hydrogen evolution experiments were performed in a 100 mL sealed quartz flask at ambient temperature and atmospheric pressure. A 300 W xenon arc lamp with lighting wavelength range of 320–780 nm (Perfectlight, PLS-SXE 300C, Beijing, China) was used as light source to trigger the photocatalytic reaction. The lamp was positioned 10 cm away from the reactor
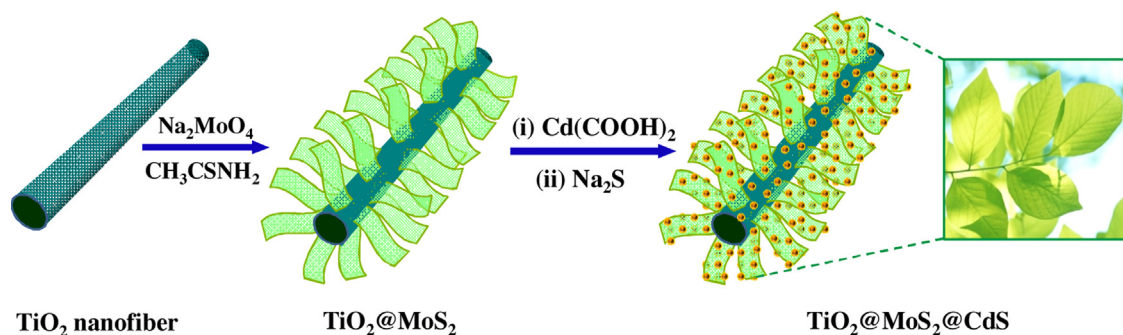
Scheme 1. Schematic illustration of the processing steps to prepare TiO$_2$@MoS$_2$@CdS "cauline-leaf"-like structure.

where the focused intensity on the flask was 160 mW cm^{-2}. In a typical photocatalytic experiment, 20 mg of photocatalysts were dispersed in an 80 mL mixed aqueous solution containing 0.35 M Na$_2$S and 0.25 M Na$_2$SO$_3$ (pH 13.2). Before irradiation, the system was bubbled with nitrogen for 30 min to remove the air ensuring the reaction system in an inertial condition. The hydrogen was analyzed by gas chromatography (Shimazu GC2010) equipped with a thermal conductive detector (TCD) and a 5 A molecular sieve column, using nitrogen as the carrier gas.

3. Results and discussion

Fig. 1a shows the field emission scanning electron microscope (FESEM) image of the calcined electrospun TiO$_2$ nanofibers with a diameter of ca. 110 nm. The surface of the TiO$_2$ nanofibers composed of TiO$_2$ particles is highly rough and porous due to the removal of PVP porogenic agents by calcination. Without using the TiO$_2$ nanofibers as growth templates, the MoS$_2$ nanosheets are clustered to form micron-sized agglomerates (Fig. 1b). The SEM image shows that the pure CdS particles in size of about 5 nm aggregate seriously (Fig. 1c). When using the TiO$_2$ nanofibers as growth templates, the few layer MoS$_2$ nanosheets vertically stand on the surface of TiO$_2$ nanofibers (Fig. 1d and e), due to the abundant pores of TiO$_2$ nanofibers which easily interact with metallic precursors. It could be interpreted by the fact: On the one hand, the rough and porous substrate of TiO$_2$ nanofibers can effectively inhibit the conformal growth of two-dimensional nanosheets on the surface of TiO$_2$ nanofibers, avoiding face-to-face stacking of MoS$_2$ nanosheets [25,26], in other words, the precursors of MoS$_2$ (sodium molybdate and thioacetamide) penetrated into the pores in TiO$_2$ nanofibers to nucleate MoS$_2$, and then the MoS$_2$ embryos grew from the inside to the outside, forming the vertical orientation and acted as nucleation centers for the growth of MoS$_2$ nanosheets; on the other hand, the roughness and surface curvature of TiO$_2$ nanofibers may be able to expand or squeeze the vertically standing molecular layers and thus change the electronic properties of the nanosheets, which may tune the HER reaction barriers effectively [27]. The noticeable curvature of the MoS$_2$ nanosheets with ripples helps to decrease the surface energy, just as in the case of graphene, implying that similar mechanisms are responsible for the stability of both two-dimensional materials [26]. The open ultrathin MoS$_2$ sheets with a high radius of curvature offer abundant surface area for the subsequent nucleation and growth of CdS nanoparticles. After in situ growth of CdS nanocrystals, the CdS nanocrystals are uniformly distributed on the surfaces of MoS$_2$ nanosheets and TiO$_2$ fiber backbone when the content of CdS in TiO$_2$@MoS$_2$@CdS is below 70 wt% (Fig. 1f–h). When increasing the content of CdS in TiO$_2$@MoS$_2$@CdS to 70 wt%, the CdS nanocrystals on MoS$_2$ nanosheets significantly aggregate and even cover MoS$_2$ sheets (Fig. 1i). Possible mechanisms of CdS growth is proposed for the strong Cd^{2+} adsorption of the layered MoS$_2$ nanosheets with negative zeta potential in TiO$_2$@MoS$_2$ het-

erostructures (Fig. S2). When S^{2-} was slowly dropped into the solution, CdS nanocrystals in-situ formed on the MoS$_2$ nanoshees of TiO$_2$@MoS$_2$ heterostructures. The average size of CdS nanoparticles in TiO$_2$@MoS$_2$@CdS is approximately 6.1 nm calculated by the Scherrer formula from the XRD analysis (Fig. S3), which agrees with the average size about 6.15 nm according to the nanoparticle size distribution (Fig. S4). Obviously, the small-size CdS nanocrystalline can more effectively capture light energy and facilitate excited electron transfer owing to the greatly reduced minority carrier diffusion distance [28].

Our studies show that the TiO$_2$@MoS$_2$@CdS containing 60 wt% CdS shows the optimal photocatalytic HER performance. Thus, the TiO$_2$@MoS$_2$@CdS in the text refers in particular to the TiO$_2$@MoS$_2$@CdS with 60 wt% CdS unless otherwise stated.

The structure of TiO$_2$@MoS$_2$@CdS was further investigated by transmission electron microscope (TEM) (Fig. 2). The TEM image of TiO$_2$@MoS$_2$@CdS displays that CdS nanoparticles are homogenously distributed on the surfaces of MoS$_2$ nanosheets (Fig. 2b). It is important to note that the CdS nanoparticle-decorated MoS$_2$ nanosheets retain vertical structure. Undoubtedly, the open and curved CdS-decorated MoS$_2$ sheets promote light harvesting, scattering and trapping, and ensure a high surface area and high density of active sites for the photocatalytic reactions [16]. The high resolution TEM (HRTEM) images of TiO$_2$@MoS$_2$@CdS clearly reveal the presence of bilayer MoS$_2$ nanosheets with inter-layer spacing of about 0.61 nm between neighboring Mo layers [29] (Fig. 2c and d). Few-layer MoS$_2$ has been proven to be conductive to photocatalytic HER due to its high electron mobility and fast electron transfer from the excited semiconductor to the catalytically active sites on MoS$_2$ [30]. The HRTEM images (Fig. 2e and f) uncover the intrinsic (1 0 0) crystal lattice of monolayer MoS$_2$ with the lattice fringe of 0.27 nm and the characteristic (1 0 1) planes of the hexagonal phase of CdS with good crystallinity which favors higher photocatalytic activity than other crystal phases [31]. The XRD patterns further confirm the existence of both hexagonal CdS and hexagonal MoS$_2$ (Fig. S3). It is worth noting that a nearly perfect transition of hexagonal CdS phase to MoS$_2$ phase is clearly observed at the interface between CdS and MoS$_2$ (Fig. 2f). Such atomically sharp contact and ultraclean interface between MoS$_2$ and CdS can minimize interface traps and non-productive recombination and ensure efficient separation and transfer of the photoexcited carriers for enhanced photocatalytic activity [32]. The energy dispersive X-ray (EDX) elemental mapping confirms that the Mo, S, and Cd are uniformly distributed in both TiO$_2$ nanofiber backbone and MoS$_2$ nanosheet branch regions whereas the Ti and O signals only exist in the TiO$_2$ nanofiber backbone region (Fig. 2g).

The chemical state of each element in composite was studied by XPS analysis. The survey spectrum as presented in Fig. 3a confirms that Ti, O, Mo, S and Cd were all presented in the TiO$_2$@MoS$_2$@CdS composite. Strong bonding among TiO$_2$, MoS$_2$ and CdS in TiO$_2$@MoS$_2$@CdS were confirmed through chemical
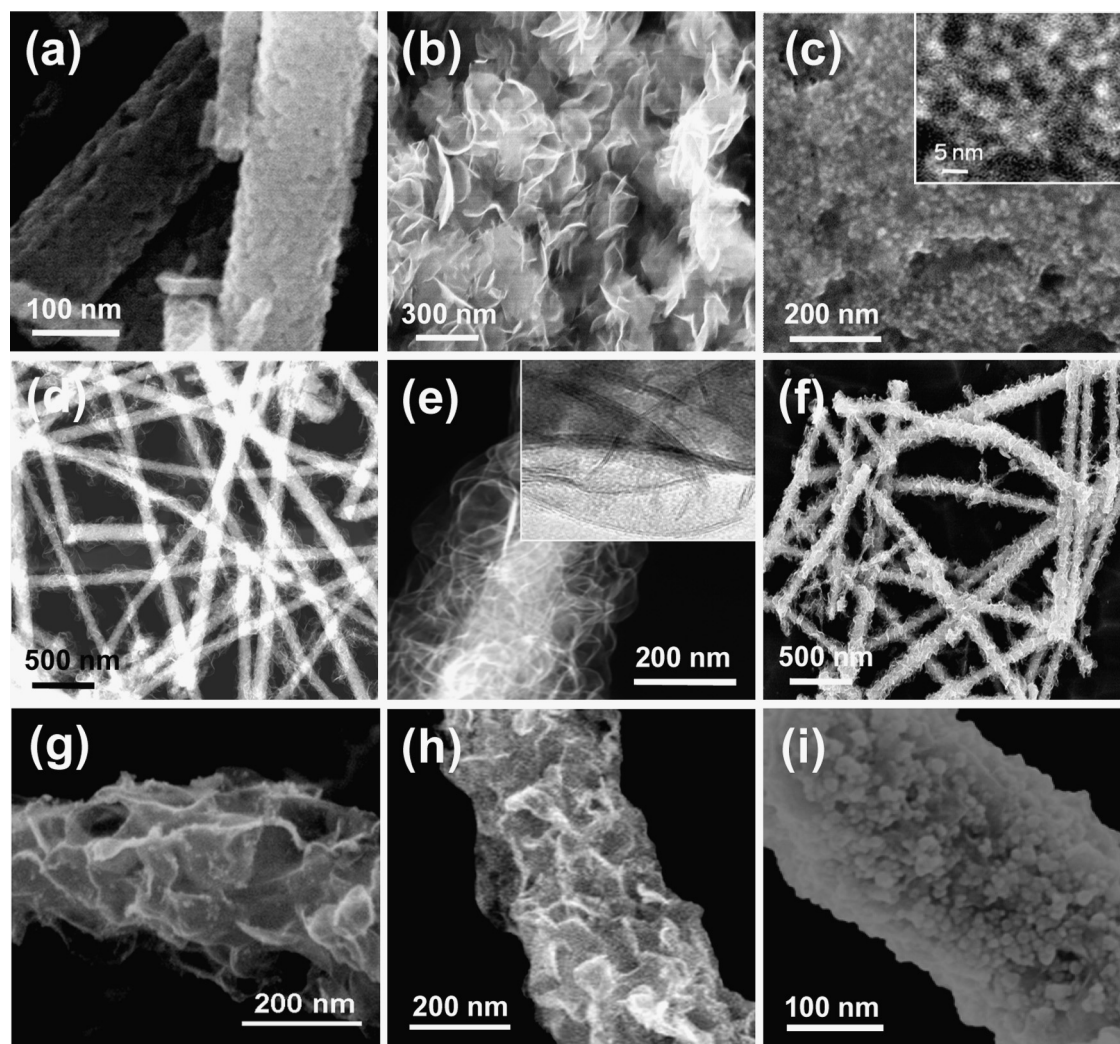
Fig. 1. SEM image of TiO_2 nanofibers (a), SEM image of pure MoS_2 sheets (b), SEM image of pure CdS in which the inset is the amplified image (c), FESEM-STEM image of $TiO_2@MoS_2$ (d), FESEM-STEM image of $TiO_2@MoS_2$ (inset is the TEM image) (e), SEM images of $TiO_2@MoS_2@CdS$ (60 wt% CdS) (f), and SEM images of $TiO_2@MoS_2@CdS$ with 50 wt% (g), 60 wt% (h), and 70 wt% CdS (i).

bonds. After MoS_2 nanosheets growing onto the TiO_2 nanofibers ($TiO_2@MoS_2$), S 2p1/2, S 2p3/2, Mo 3d3/2 and Mo 3d5/2 peaks shifted to 162.9, 161.9, 232 and 228.8 eV, respectively, lower than those of pure MoS_2 (Fig. 3b and c). $TiO_2@MoS_2@CdS$ showed the characteristic oxidation state (Cd^{2+}) with featured peaks of 405.24 eV (Cd 3d 5/2) and 411.98 eV (Cd 3d 3/2) (Fig. 3d), respectively, higher than those of pure CdS. The shift of binding energies means electronic interactions between MoS_2 and CdS.

The porous structure of all the samples were determined by N_2 adsorption-desorption isotherm method based on Brunauer–Emmett–Teller (BET) analysis (Fig. S5 and Table S1). The specific surface areas of $TiO_2@MoS_2@CdS$, $TiO_2@MoS_2$ and pure CdS are 97, 27 and 43 $m^2\,g^{-1}$, respectively. The large surface area of $TiO_2@MoS_2@CdS$ attributes to the freely suspended atomically-thin MoS_2 nanosheets and the fully exposed CdS nanocrystal particles. Obviously, this "cauline leaf"-like structure of $TiO_2@MoS_2@CdS$ is thoroughly accessible to both light irradiation and electrolyte reactants, ideal for the photocatalytic H_2 evolution activity.

UV–vis diffuse reflectance spectra (DRS) reveal that pure CdS exhibits the inherent visible-light absorption [33] whereas $TiO_2@MoS_2$ and $TiO_2@MoS_2@CdS$ show the characteristic absorptions of monolayer MoS_2 at about 630 nm [34] and that of anatase TiO_2 at 380 nm, respectively (Fig. 4a). Compared with CdS and

TiO_2 alone, the MoS_2-containing photocatalysts exhibit significant absorption in the entire visible range because of the strong light scattering and trapping effect from MoS_2 nanosheets. It is emphasized that $TiO_2@MoS_2$ and $TiO_2@MoS_2@CdS$ still show strong absorptions in UV region (<400 nm), revealing that the open vertical MoS_2 or $MoS_2@CdS$ make limited obstruction on the light absorption of TiO_2 nanofiber core. Photocurrent is commonly adopted to evaluate the ability of producing and separating charge carriers in photocatalysts [35]. The photocurrent density of $TiO_2@MoS_2@CdS$ is much higher than those of other samples at zero bias potential, indicating notable improvement in photo-carrier generation, separation and extraction (Fig. 4b and inset). Meanwhile, $TiO_2@MoS_2@CdS$ shows a more negative shift of the zero-current potential, further confirming the better separation of the photo-generated electrons and holes of $TiO_2@MoS_2@CdS$.

The photocatalytic hydrogen production activities of $TiO_2@MoS_2@CdS$, TiO_2 nanofibers, $TiO_2@MoS_2$, $CdS@MoS_2$, CdS and the physical mixture of $TiO_2@MoS_2$ and CdS were measured under simulated solar light or visible light irradiation and compared in Fig. 5a. Obviously, the hydrogen production rates over all $TiO_2@MoS_2@CdS$ hybrids are much higher than those over other photocatalysts. For $TiO_2@MoS_2@CdS$, CdS exhibits an important influence on the photocatalytic activity. The highest hydrogen production rates are observed over the $TiO_2@MoS_2@CdS$
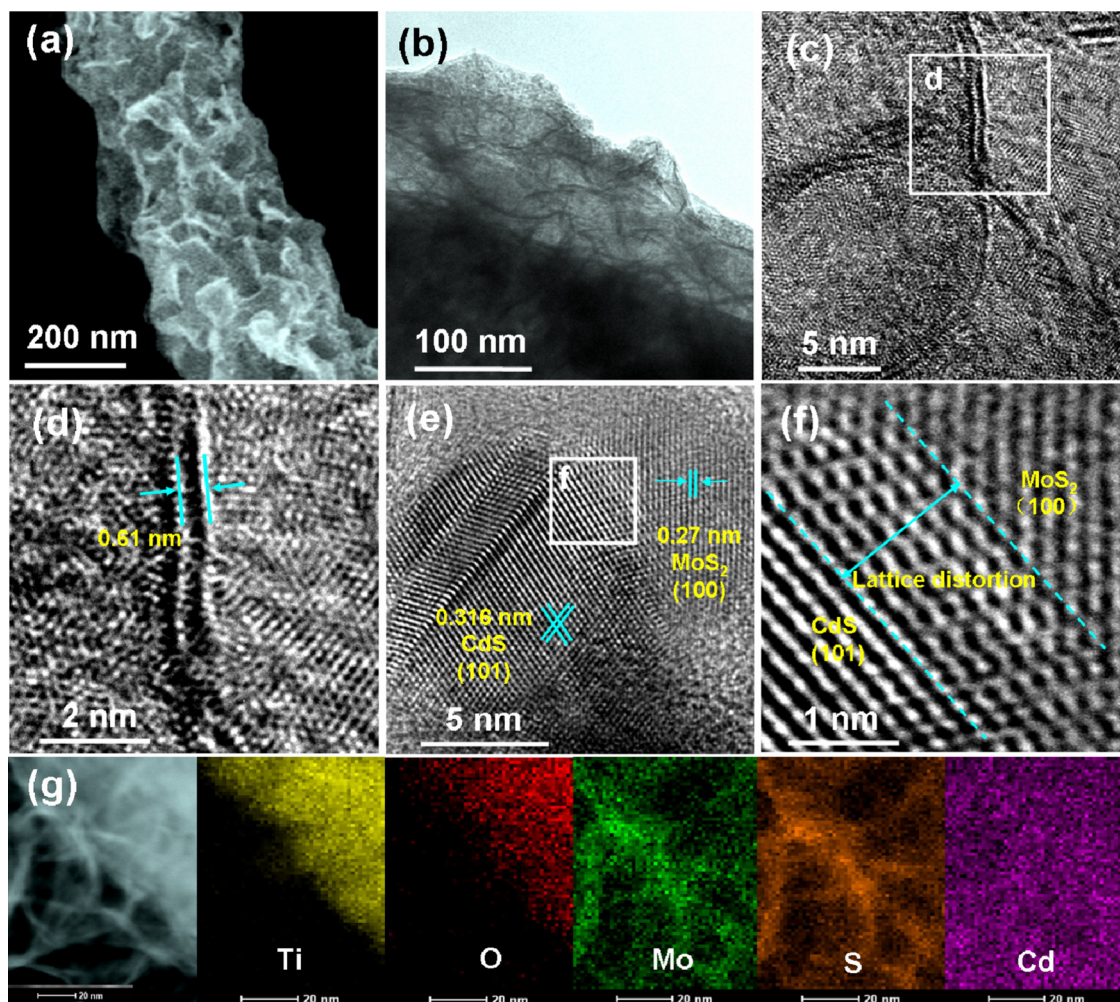
Fig. 2. (a) SEM image of TiO$_2$@MoS$_2$@CdS, (b) TEM image of TiO$_2$@MoS$_2$@CdS, (c) HRTEM image of TiO$_2$@MoS$_2$@CdS, (d) amplified HRTEM image of designated square part in (c), (e) HRTEM image of TiO$_2$@MoS$_2$@CdS, (f) amplified HRTEM image of designated square part in (e), and (g) EDS elemental mappings of TiO$_2$@MoS$_2$@CdS.
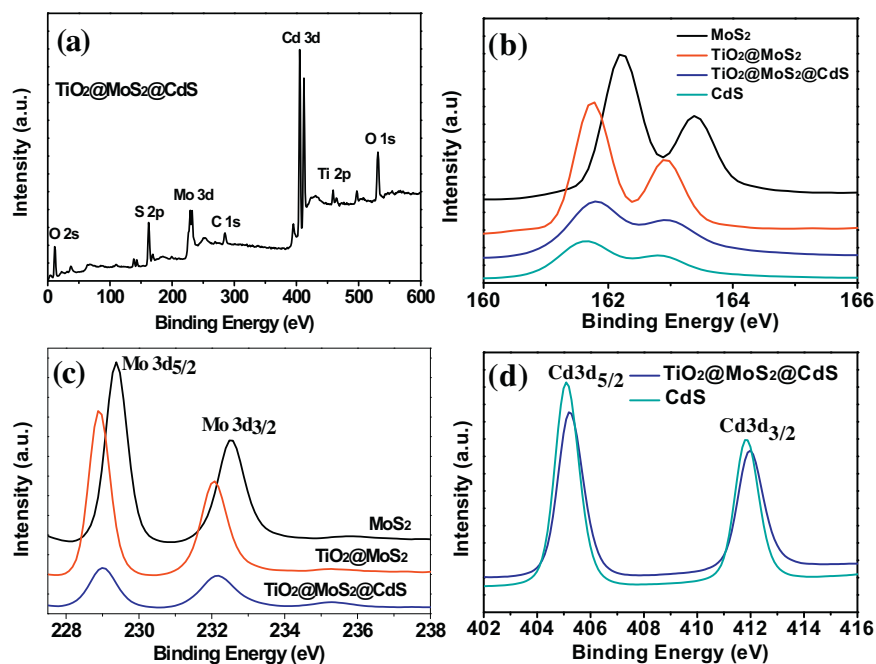
Fig. 3. XPS spectra of the samples: (a) XPS full survey spectrum of TiO$_2$@MoS$_2$@CdS; (b) S2p peaks of pure MoS$_2$, TiO$_2$@MoS$_2$, TiO$_2$@MoS$_2$@CdS and CdS; (c) Mo3d peaks of pure MoS$_2$, TiO$_2$@MoS$_2$,TiO$_2$@MoS$_2$@CdS; (d) Cd3d peaks of TiO$_2$@MoS$_2$@CdS and CdS.
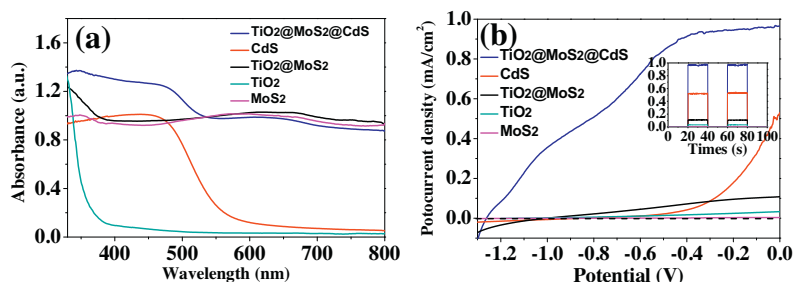
Fig. 4. (a) UV–vis diffuse-reflectance spectra of different samples. (b) Photocurrent–voltage characteristics of the samples deposited on FTO electrode in aqueous solution (pH 13.2, 0.35 M Na$_2$S, 0.25 M Na$_2$SO$_3$) at different bias potentials, with a platinum foil as the counter electrode and a saturated calomel electrode (SCE) as the reference electrode. The inset in (b) is the photocurrent at zero bias potential under time-dependent light irradiation.

with 60 wt% of CdS, corresponding to 12.3 or 6.2 mmol h^{-1} g^{-1} under simulated solar light or visible light irradiation. Decreasing CdS to 50 wt% and 0 wt% in TiO$_2$@MoS$_2$@CdS, the hydrogen production rates decrease to 9.3 or 4.2 mmol h^{-1} g^{-1} (50 wt%) and 1.7 or 0.5 (0 wt%, namely TiO$_2$@MoS$_2$) under simulated solar light or visible light irradiation, whereas increasing CdS to 70 wt% in TiO$_2$@MoS$_2$@CdS, the hydrogen production rates decrease to 11.4 or 5.8 mmol h^{-1} g^{-1}. Too low CdS loading causes the poor light absorption, while excess CdS coating blocks the light from reaching the TiO$_2$ nanofibers, thus weakening the generation of photogenerated electrons/holes in TiO$_2$. Also, the excessive accumulation of CdS nanoparticles on MoS$_2$ nanosheets (Fig. 1i) could reduce the charge transfer efficiency and/or cover the catalytically active sites in MoS$_2$ nanosheets. The photocatalytic hydrogen production activity of CdS@MoS$_2$ with the optimum amount of 95 wt% CdS has been investigated. Compared with pure and free MoS$_2$ templates which would tend to gather, the ultrathin MoS$_2$ nanosheets that were vertically immobilized on the rough and porous substrate of TiO$_2$ nanofibers had the bigger surface area and much more content of vacancies that were more amenable to nucleation for CdS. So, photocatalytic H$_2$ production activities of TiO$_2$@MoS$_2$@CdS were much higher than that of CdS@MoS$_2$. For TiO$_2$ and CdS alone, their low hydrogen production rates are due to the rapid recombination of photoinduced carriers or lack of HER active centers. For TiO$_2$@CdS, low hydrogen production rate was caused by lack of the efficient cocatalyts as HER active centers while for TiO$_2$@MoS$_2$@CdS, the atomically-thin MoS$_2$ had more exposed edges and unsaturated active S atoms, resulting in the higher HER activity. For MoS$_2$ alone, low hydrogen production rates were also observed. The low activity of solitary MoS$_2$ should be ascribed to either its limited photogenerated charges or the photogenerated charges could not efficiently migrate to the exposed HER-active edges due to the serious aggregation [36]. In addition, the physical mixture of 40 wt% TiO$_2$@MoS$_2$ and 60 wt% CdS also shows relatively low hydrogen production rates of 1.0 or 0.4 mmol h^{-1} g^{-1} under simulated solar light or visible light irradiation. It can be attributed to the fact that the physical mixture results in the poor electrical contact between the two components with rather inefficient interface charge transfer.

The apparent quantum efficiency (AQE) for TiO$_2$@MoS$_2$@CdS was calculated according to Eq. (1). The calculated AQEs reach 70.5% or 57.6% at 365 or 420 nm.

$$AQE(\%) = \frac{\text{Number of reacted electrons}}{\text{Number of incident photons}} \times 100$$
$$= \frac{\text{Number of evolved H}_2 \text{ molecules} \times 2}{\text{Number of incident photons}} \times 100 \quad (1)$$

Although the direct comparison of different photocatalysts for photocatalytic HER is difficult due to different experiment conditions, the AQEs and H$_2$ evolution rates of photocatalysts

could reflect the ability of photocatalytic HER. Table S2 lists the photocatalytic hydrogen evolution behavior of MoS$_2$-based or CdS-based photocatalysts reported in recent years. The hybrid photocatalyst exhibits high hydrogen production rates up to 12.3 or 6.2 mmol h^{-1} g^{-1} under simulated solar light or visible light irradiation and high apparent quantum efficiencies of 70.5% at 365 nm or 57.6% at 420 nm, representing one of the best reported HER photocatalysts, which compares well with those with noble-metal cocatalysts. The outstanding photocatalytic hydrogen evolution reaction activity should be attributed to the unique "cauline leaf"-like architecture of the photocatalyst for omnidirectionally enhancing photocatalytic hydrogen evolution.

The stability of photocatalytic activity of TiO$_2$@MoS$_2$@CdS was also evaluated by reusing the photocatalyst for multiple hydrogen evolution reaction cycles. Six consecutive photocatalytic reactions were performed under simulated solar light or visible light irritation (Fig. 5b). The amount of generated hydrogen increases steadily with the irradiation time in each cycle. More importantly, the hybrid photocatalyst remains highly stable after a long-time test (30 h) and the hydrogen production rates in the sixth cycle remain nearly the same as those in the first cycle, demonstrating the exceptional photocatalytic stability of the hybrid photocatalysts.

To further understand the reason for the drastically enhanced photocatalytic activity of TiO$_2$@MoS$_2$@CdS for H$_2$ evolution as compared to CdS@MoS$_2$ and pure CdS, steady-state photoluminescence (PL) and time-resolved transient PL decay spectra were carried out to elucidate the formation and migration dynamic behavior of photogenerated charge carriers in the as-fabricated photocatalysts (Fig. 6). All the samples were excited by 400 nm only to excite CdS illumination without the interference of TiO$_2$. The PL emission of CdS@MoS$_2$ and TiO$_2$@MoS$_2$@CdS was remarkably quenched, revealing that the unwanted charge recombination process could be suppressed by the presence of MoS$_2$. It is interesting that the PL intensity of TiO$_2$@MoS$_2$@CdS is much smaller than that of CdS@MoS$_2$. To gain more understanding on this phenomenon, the time-resolved photoluminescence (TRPL) spectrum decay curves were fitted by exponential decay kinetics function expressed as follows:

$$I(t) = A_1(\exp -t/\tau_1) + A_2(\exp -t/\tau_2) + A_3(\exp -t/\tau_3) \quad (2)$$

Meanwhile, the average emission lifetime, reflecting the overall emission decay behavior of samples, was also calculated through the following equation:

$$\tau_A = \frac{A_1\tau_1^2 + A_2\tau_2^2 + A_3\tau_3^2}{A_1\tau_1 + A_2\tau_2 + A_3\tau_3} \quad (3)$$

where τ_1, τ_2, and τ_3 are the emission lifetimes, and A_1, A_2, and A_3 are the corresponding amplitudes. As listed in Table 1, the longer lifetime component, τ_1, is caused by the free excitons recombination in the CdS while the short life-time components, τ_2 and τ_3, are originated from the non-radiative recombination of charge carriers in
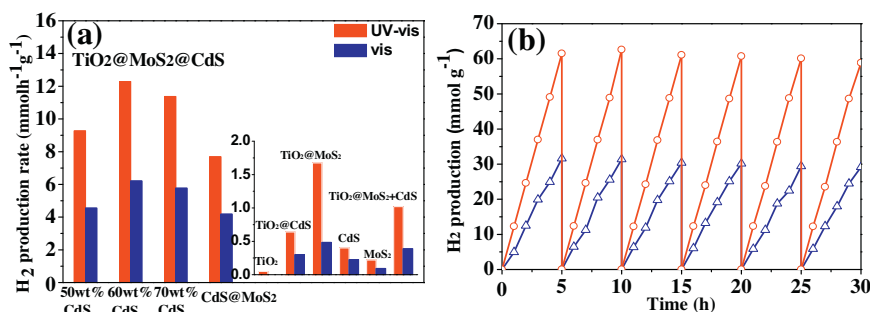
Fig. 5. (a) The photocatalytic hydrogen production activities of $TiO_2@MoS_2@CdS$ (50, 60, and 70 wt% CdS) and $CdS@MoS_2$ with the optimum amount of 95 wt% CdS under simulated solar light (320–780 nm) or visible light (>420 nm) irradiation at zero potential. The reaction was conducted with 20 mg of photocatalysts in an 80 mL mixed aqueous solution (pH 13.2, 0.35 M Na_2S, 0.25 M Na_2SO_3). The inset in (a) is the photocatalytic hydrogen production activities of TiO_2 nanofibers, $TiO_2@CdS$, $TiO_2@MoS_2$, CdS, MoS_2 nanosheets and the physical mixture of 40 wt% $TiO_2@MoS_2$ and 60 wt% CdS. (b) Repeated H_2 evolution cycles catalyzed by $TiO_2@MoS_2@CdS$ (60 wt% CdS) under simulated solar light (red) and visible light irradiation (blue). (For interpretation of the references to color in this figure legend, the reader is referred to the web version of this article.)
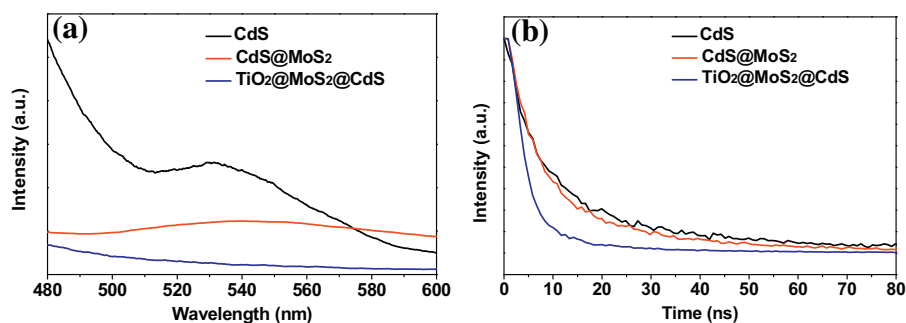

Fig. 6. (a) Steady-state PL and (b) time-resolved transient PL decay spectra of pure CdS, $CdS@MoS_2$ and $TiO_2@MoS_2@CdS$.

Table 1
Dynamics analysis of emission decay for the different samples.

Samples	A_1 (%)	τ_1 (ns)	A_2 (%)	τ_2 (ns)	A_3 (%)	τ_3 (ns)	τ_A (ns)
CdS	9.8	10.6	46.2	2.5	44.0	0.65	5.68
$MoS_2@CdS$	9.4	6.7	45.5	1.6	45.1	0.48	3.49
$TiO_2@MoS_2@CdS$	4.5	4.7	32.9	0.38	62.6	0.38	1.97

the surface defect states. It is clearly seen that the emission lifetime of CdS was decreased from 5.68 to 3.49 ns when integrating it with MoS_2 to form the heterostructure. Furthermore, after loading CdS onto $TiO_2@MoS_2$ heterostructure, the emission lifetime of the sample was further decreased to 1.97 ns which are 1.77 and 2.88 times shorter than those of $CdS@MoS_2$ and CdS, respectively. The reduced decay lifetime and quenched PL suggest the more effective charge-carrier formation and faster interfacial charge transfer occurring in the hetero-nanostructural photocatalyst due to the emergence of non-radiative quenching pathways. The dynamics process of photoinduced charge carriers can be further deduced through the electron transfer rate constants (K_{et}) expressed as follows:

$$K_{et}(CdS@MoS_2 \rightarrow CdS) = \frac{1}{\langle \tau_A \rangle (CdS@MoS_2)} - \frac{1}{\langle \tau_A \rangle (CdS)} \quad (4)$$

$$K_{et}(TiO_2@MoS_2@CdS \rightarrow CdS) = \frac{1}{\langle \tau_A \rangle (TiO_2@MoS_2@CdS)} - \frac{1}{\langle \tau_A \rangle (CdS)} \quad (5)$$

According to the energy band structures of CdS and MoS_2, the rate constant of photoinduced electrons transferring from the conduction band (CB) of CdS to the CB of MoS_2 could be estimated, which are about 1.1×10^8 s^{-1} and 3.3×10^8 s^{-1} for the $CdS@MoS_2$ and $TiO_2@MoS_2@CdS$ samples, respectively. In the case

of $TiO_2@MoS_2@CdS$, the larger rate constant for electron dynamics process could be mainly caused by the fewer layer number of MoS_2. On the one hand, the much stronger coupling effect between ultrathin MoS_2 sheets and CdS nanoparticles could contribute to the efficient charge transfer and suppression of the electron–hole recombination. On the other hand, the much thinner MoS_2 layers has much more active sites or higher electrical conductivity for promoting the photoinduced electron migration and boosting the photoinduced electron production.

The photocatalytic HER mechanism is proposed in Fig. 7a. The schematic illustration of separation of photoinduced electron–hole pairs in $TiO_2@MoS_2@CdS$ is presented. The band gap of CdS is about 2.40 eV, and the conduction band (CB) and valence band (VB) energy levels of CdS are about −0.50 and 1.90 eV vs. SHE, respectively. The CB and VB energy levels of $TiO2$ are about −0.26 and 2.94 eV vs. SHE, respectively. The CB and VB energy levels of $MoS2$ are about −0.12 and 1.78 eV vs. SHE as a result of the quantum-confinement effect [25]. The conduction band (CB) in MoS_2 is lower than that TiO_2 and CdS. Under simulated solar light illumination, the valence band electrons in both TiO_2 and CdS were excited to their conduction bands, and then immediately transferred to MoS_2 for H_2 evolution [37]. The sacrificial reagent would complement the electrons to the remaining holes in the VB of $TiO_2@MoS_2@CdS$. The edge of MoS_2 sheets with unsaturated active S atoms that have strong bonds to H$^+$ in the solution are over entire surface of the catalytic
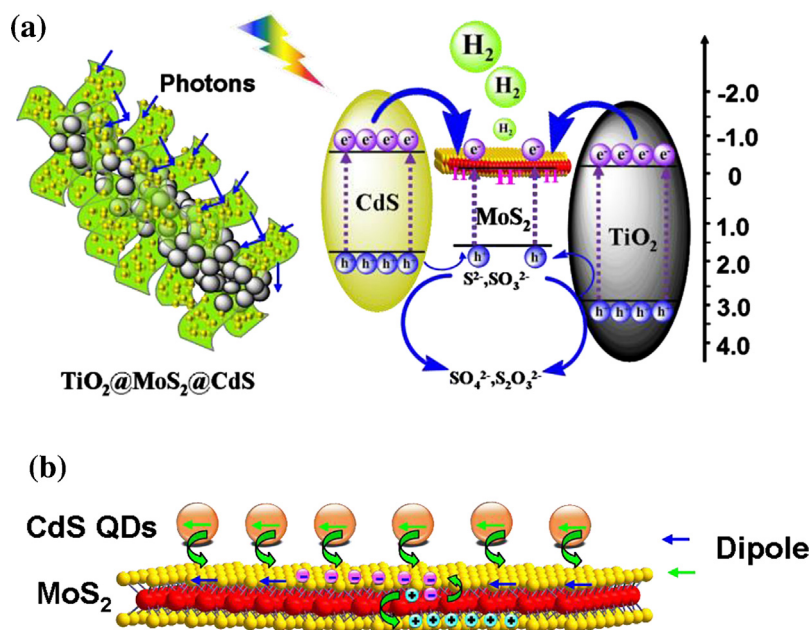
Fig. 7. (a) Illustration of the HER mechanism over TiO_2@MoS_2@CdS under simulated solar light irradiation. (b) Schematic picture of CdS sensitized 2-D MoS_2 nanoshees (nonradiative energy transfer from CdS to MoS_2 nanosheets).

support surface and the edges of MoS_2 sheets can accept photogenerated electrons and act as active sites for H_2 generation. MoS_2 is involved in different energy transfer mechanisms, which significantly enhances the photocatalytic activity. The vertically standing MoS_2 sheets can not only maximally expose active sites for effective HER but also reduce gas bubble adhesion for offering constant working area [38]. Additionally, the scattering of photons among MoS_2 nanosheets increases the effective photon path length, producing more photogenerated carriers [16,39]. There is a possible mechanism need to be further confirmed (Fig. 7b). MoS_2 can be sensitized by CdS to create a hybrid energy transfer architecture. The in-plane oriented dipole moments from monolayer MoS_2 and CdS are strongly coupled. Nonradiative energy transfer from CdS to MoS_2 is enhanced due to the reduced dielectric screening of in-plane components of the donor dipole field. More free electrons and holes will be generated, thus leading to higher HER efficiencies [40,41]. Lastly, this "cauline leaf"-like structure is thoroughly accessible to reactants. Together, the well-designed "cauline leaf" structure cannot only promote efficient photon absorption, charge generation and separation, but also ensure highly efficient utilization of the charge carriers for effective HER and enhanced H_2 evolution rates.

4. Conclusions

In summary, we have demonstrated a simple technique to synthesize a hierarchical "cauline leaf" nanoarchitecture with vertically standing atomically-thin MoS_2 nanosheets on TiO_2 nanofibers, and uniformly decorated CdS nanocrystals. The hybrid photocatalyst exhibits high hydrogen production rates up to 12.3 or 6.2 mmol h^{-1} g^{-1} under simulated solar light or visible light irradiation and high apparent quantum efficiencies of 70.5% at 365 nm or 57.6% at 420 nm, representing one of the best reported HER photocatalysts. It is also important to note that the hybrid photocatalysts remain highly stable after a continued test for 30 h. The outstanding HER performance is ascribed to omnidirectional enhancement of optical absorption and charge transfer across the unique "cauline leaf" ensemble. This study could open new opportunities for the rational design and a better understanding of structure-property relationships of hierarchical nanoarchitectures for photocatalytic water splitting and solar fuel generation.

Appendix A. Supplementary data

Supplementary data associated with this article can be found, in the online version, at http://dx.doi.org/10.1016/j.apcatb.2015.12.056.

References

[1] C.A. Rodriguez, M.A. Modestino, D. Psaltis, C. Moser, Energy Environ. Sci. 7 (2014) 3828–3835.
[2] L.P. Hansen, Q.M. Ramasse, C. Kisielowski, M. Brorson, E. Johnson, H. Topsoe, S. Helveg, Angew. Chem. Int. Ed. 50 (2011) 10153–10156.
[3] J.R. McKone, A.P. Pieterick, H.B. Gray, N.S. Lewis, J. Am. Chem. Soc. 135 (2012) 223–231.
[4] A.B. Laursen, S. Kegnæs, S. Dahl, I. Chorkendorff, Energy Environ. Sci. 5 (2012) 5577–5591.
[5] M. Chhowalla, H.S. Shin, G. Eda, L.J. Li, K.P. Loh, H. Zhang, Nat. Chem. 5 (2013) 263–275.
[6] C.G. Morales-Guio, S.D. Tilley, H. Vrubel, M. Grätzel, X. Hu, Nat. Commun. 5 (2014), http://dx.doi.org/10.1038/ncomms4059.
[7] J. Kibsgaard, Z. Chen, B.N. Reinecke, T.F. Jaramillo, Nat. Mater. 11 (2012) 963–969.
[8] H.I. Karunadasa, E. Montalvo, Y. Sun, M. Majda, J.R. Long, C.J. Chang, Science 335 (2012) 698–702.
[9] B. Lassalle-Kaiser, D. Merki, H. Vrubel, S. Gul, V.K. Yachandra, X. Hu, J. Yano, J. Am. Chem. Soc. 137 (2015) 314–321.
[10] Y.Q. Qu, L. Liao, R. Cheng, Y. Wang, Y.C. Lin, Y. Huang, X.F. Duan, Nano Lett. 10 (2010) 1941–1949.
[11] H.L. Zhou, Y.Q. Qu, T. Zeid, X.F. Duan, Energy Environ. Sci. 5 (2012) 6732–6743.
[12] Y.Q. Qu, X.F. Duan, Chem. Soc. Rev. 42 (2013) 2568–2580.
[13] H.Y. Wang, F. Qian, G.M. Wang, Y.Q. Jiao, Z. He, Y. Li, ACS Nano 7 (2013) 8728–8735.
[14] C.L. Tan, H. Zhang, Chem. Soc. Rev. 44 (2015) 2713–2731.
[15] X. Li, J.Q. Yu, J.X. Low, Y.P. Fang, J. Xiao, X.B. Chen, J. Mater. Chem. A 3 (2015) 2485–2534.

[16] W.Q. Wu, H.L. Feng, H.S. Rao, Y.F. Xu, D.B. Kuang, C.Y. Su, Nat. Commun. 5 (2014) 3968–3977.
[17] B. Mahler, V. Hoepfner, K. Liao, G.A. Ozin, J. Am. Chem. Soc. 136 (2014) 14121–14127.
[18] Y.J. Yuan, Z.T. Yu, X.J. Liu, J.G. Cai, Z.J. Guan, Z.G. Zou, Sci. Rep. 4 (2014) 4045–4052.
[19] J.Z. Chen, X.J. Wu, L.S. Yin, B. Li, X. Hong, Z.X. Fan, B. Chen, C. Xue, H. Zhang, Angew. Chem. Int. Ed. 53 (2014) 1226–1230.
[20] K. Chang, Z.W. Mei, T. Wang, Q. Kang, S.X. Ouyang, J.H. Ye, ACS Nano 8 (2014) 7078–7087.
[21] J.H. Liu, L. Zhang, N.X. Li, Q.W. Tian, J.C. Zhou, Y.M. Sun, J. Mater. Chem. A 3 (2015) 706–712.
[22] F.K. Meng, J.T. Li, S.K. Cushing, M.J. Zhi, N.Q. Wu, J. Am. Chem. Soc. 135 (2013) 10286–10289.
[23] J. Kibsgaard, T.F. Jaramillo, F. Besenbacher, Nat. Chem. 6 (2014) 248–253.
[24] W.J. Zhou, Z.Y. Yin, Y.P. Du, X. Huang, Z.Y. Zeng, Z.X. Fan, H. Liu, J.Y. Wang, H. Zhang, Small 9 (2013) 140–147.
[25] C. Liu, L. Wang, Y. Tang, S. Luo, Y. Liu, S. Zhang, Y. Zeng, Y. Xu, Appl. Catal. B Environ. 164 (2015) 1–9.
[26] H.T. Wang, D.S. Kong, P. Johanes, J.J. Cha, G.Y. Zheng, K. Yan, N. Liu, Y. Cui, Nano Lett. 13 (2013) 3426–3433.
[27] J. Brivio, D.T. Alexander, A. Kis, Nano Lett. 11 (2011) 5148–5153.
[28] V.I. Klimov, S.A. Ivanov, J. Nanda, M. Achermann, I. Bezel, J.A. McGuire, A. Piryatinski, Nature 447 (2007) 441–446.
[29] K.H. Liu, L.M. Zhang, T. Cao, C.H. Jin, D. Qiu, Q. Zhou, A. Zettl, P.D. Yang, S.G. Louie, F. Wang, Nat. Commun. 5 (2014).
[30] K. Chang, M. Li, T. Wang, S.X. Ouyang, P. Li, L.Q. Liu, J.H. Ye, Adv. Energy Mater. (2015), http://dx.doi.org/10.1002/aenm.201402279.
[31] N.Z. Bao, L.M. Shen, T. Takata, K. Domen, A. Gupta, K. Yanagisawa, C.A. Grimes, J. Phys. Chem. C 111 (2007) 17527–17534.
[32] J.H. Yang, D. Wang, H.X. Han, C. Li, Acc. Chem. Res. 46 (2013) 1900–1909.
[33] Q. Li, B.D. Guo, J.G. Yu, J.R. Ran, B.H. Zhang, H.J. Yan, J.R. Gong, J. Am. Chem. Soc. 133 (2011) 10878–10884.
[34] E.S. Kadantsev, P. Hawrylak, Solid State Commun. 152 (2012) 909–913.
[35] R.M. Ribeiro, A. Eckmann, R. Jalil, B.D. Belle, A. Mishchenko, Y.J. Kim, R.V. Gorbachev, T. Georgiou, S.V. Morozov, A.N. Grigorenko, A.K. Geim, C. Casiraghi, A.H. Castro Neto, K.S. Novoselov, Science 340 (2013) 1311–1314.
[36] Q.J. Xiang, J.G. Yu, M. Jaroniec, J. Am. Chem. Soc. 134 (2012) 6575–6578.
[37] Y.Q. Guo, K. Xu, C.Z. Wu, J.Y. Zhao, Y. Xie, Chem. Soc. Rev. 44 (2015) 637–646.
[38] Z.Y. Lu, W. Zhu, X.Y. Yu, H.C. Zhang, Y.J. Li, X.M. Sun, X.W. Wang, H. Wang, J.M. Wang, J. Luo, X.D. Lei, L. Jiang, Adv. Mater. 26 (2014) 2683–2687.
[39] M. Zhou, X.W. Lou, Y. Xie, Nano Today 8 (2013) 598–618.
[40] F. Prins, A.J. Goodman, W.A. Tisdale, Nano Lett. 14 (2014) 6087–6091.
[41] B. Peng, P.K. Ang, K.P. Loh, Nano Today 10 (2015) 128–137.